NJC

Accepted Manuscript

This is an *Accepted Manuscript*, which has been through the Royal Society of Chemistry peer review process and has been accepted for publication.

Accepted Manuscripts are published online shortly after acceptance, before technical editing, formatting and proof reading. Using this free service, authors can make their results available to the community, in citable form, before we publish the edited article. We will replace this *Accepted Manuscript* with the edited and formatted *Advance Article* as soon as it is available.

You can find more information about *Accepted Manuscripts* in the Information for Authors.

Please note that technical editing may introduce minor changes to the text and/or graphics, which may alter content. The journal's standard Terms & Conditions and the Ethical guidelines still apply. In no event shall the Royal Society of Chemistry be held responsible for any errors or omissions in this *Accepted Manuscript* or any consequences arising from the use of any information it contains.

ROYAL SOCIETY OF CHEMISTRY

www.rsc.org/njc

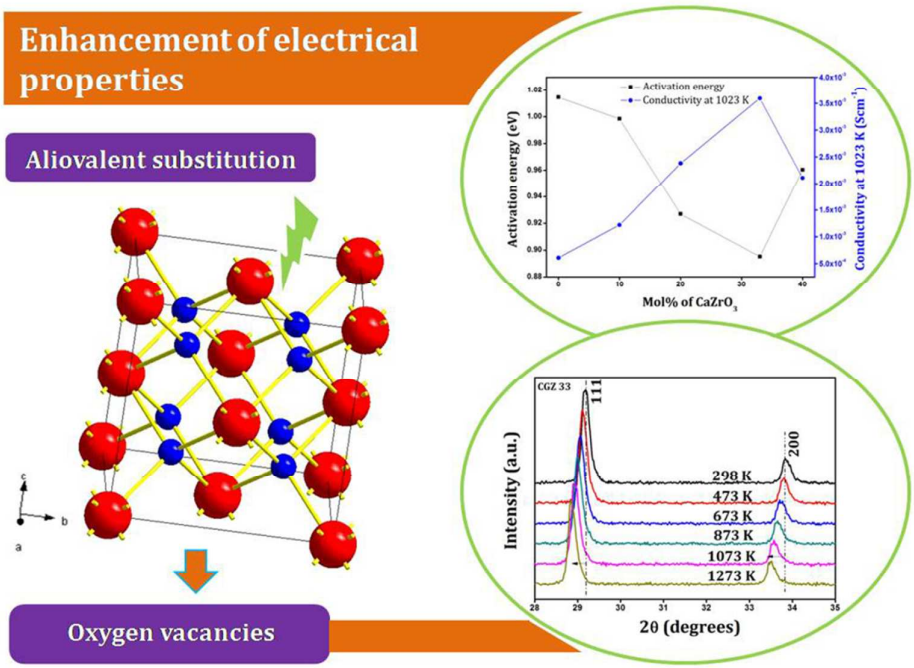

A stoichiometry involving *x*% $CaZrO_3$ and *(100-x)*% $Gd_2Zr_2O_7$ was found to enhance the electrical properties of $Gd_2Zr_2O_7$ through induced oxygen vacancies.

Induced Oxygen Vacancies and their effect on the Structural and Electrical properties of Fluorite-type $CaZrO_3$-$Gd_2Zr_2O_7$ system

Vaisakhan Thampi, Prabhakar Rao Padala*, Radhakrishnan A N

Materials Science and Technology Division, National Institute for Interdisciplinary Science and Technology (NIIST), Trivandrum, India-695019

*Corresponding author. Tel.: + 91 471 2515311; Fax: + 91 471 2491712

E-mail: padala_rao@yahoo.com

Abstract:

Solid oxide materials were prepared via solid state reaction route with a stoichiometry composition: *x*% of $CaZrO_3$ and *(100-x)*% of $Gd_2Zr_2O_7$ (*x* = 10, 20, 33.3, 40). Powder X-ray diffraction in ambient and high-temperature conditions, scanning electron microscopy, transmission electron microscopy and ac impedance spectroscopy techniques were used to analyze and correlate the structural and electrical properties of the materials. The aliovalent substitution of Gd^{3+} by Ca^{2+} allowed creation of more oxygen vacancies in the lattice of these compositions. This resulted into a progressive decrease in lattice parameter and an increase in thermal expansion coefficient. The induced oxygen vacancies provided a lower energy barrier for ionic diffusion and hence led to an increase in conductivity which was found to show a maximum value of 3.59 $x10^{-3}$ Scm^{-1} at 1023 K for *x* = 33.3. The high ionic conductivity value measured in this study indicates that the solid solutions of this kind are promising to be good ionic conductors.

Keywords: Gadolinium zirconate; Solid oxide electrolyte; Electrical conductivity; Solid oxide fuel cells

1. Introduction:

Search for efficient solid oxide electrolytes for solid oxide fuel cell (SOFC) applications is gaining much attention nowadays. In this respect, rare earth zirconates of the type $RE_2Zr_2O_7$

are being explored extensively[1-4] which are found to exhibit a lot of interesting properties from the view of their high melting point, thermal stability, thermal expansion coefficient etc. They possess a defect pyrochlore or defect fluorite type crystal structure which are capable of accommodating comparatively large amount of oxygen non-stoichiometry helpful for effective ionic diffusion in a solid electrolyte. Many attempts to enhance their ionic conductivity by doping with aliovalent or isovalent elements to RE or Zr sites have been reported.[5-9]

Among the various zirconate systems reported, $Gd_2Zr_2O_7$ is found to be a very good candidate owing to its high electrical conductivity.[10-12] From crystallographic point of view, it is known to exist in two different space groups depending on the conditions of preparation.[13] If annealed at a temperature above 1773 K, it attains an anion-deficient fluorite structure with space group Fm3m, whereas below 1773 K, it normally exists as a disordered pyrochlore with space group Fd3m.[13] An investigation on the effect of Eu^{3+} substitution in place Gd^{3+} done by Xia et al.[10] showed that the ionic conductivity of $Gd_2Zr_2O_7$ increases with increase in Eu^{3+} content. A similar substitution of Gd^{3+} with Sm^{3+} in $Gd_{2-x}Sm_xZr_2O_7$ system was studied by Liu et al and they found $GdSmZr_2O_7$ (x = 1) to be the best among them in terms of ionic conductivity.[11, 12] Later they studied the effect of CaO addition in the $GdSm_{1-x}Ca_xZr_2O_7$ ($0 \leq x \leq 0.20$) system[14] and reported that addition of CaO could increase the ionic conductivity of the system up to x = 0.10. But, towards higher concentrations, CaO was found to decrease the conductivity of the system by enhancing the formation of $CaZrO_3$ secondary phase. Xia et al.[15] had already studied the effect of CaO on $(Sm_{1-x}Ca_x)_2Zr_2O_7$ system and reported that formation of poorly conducting $CaZrO_3$ phase is detrimental to the ionic conductivity of the system. Aliovalent substitutions can cause interstitial or vacant anionic sites in order for the requirement of electroneutrality and this can crucially influence various physical properties of the materials.[16-19] Inducing oxygen vacancies can create an easy pathway for ionic diffusion

through a crystal lattice thereby making it a better conductor. This is also reported to influence the thermal expansion behaviour of solid oxide materials.[20-22] Hence it should be inferred that addition of divalent Ca can influence the ionic conductivity positively, provided it does not lead to the formation of poorly conducting secondary phases.

Here in this work an attempt to add more Ca^{2+} to $Gd_2Zr_2O_7$ without the formation of secondary phases has been made. Solid solutions were prepared by proposing a stoichiometry of $x CaZrO_3$-$(1-x)Gd_2Zr_2O_7$ and their structural and electrical characteristics were investigated.

2. Experimental:

For brevity, the proposed chemical systems in the present work will be designated as GZ, CGZ 10, CGZ 20, CGZ 33 and CGZ 40 where GZ stands for $Gd_2Zr_2O_7$ and the numeral following CGZ represents the value of the particular percentage (x) in $x\%CaZrO_3$ - $(100-x)\%Gd_2Zr_2O_7$ stoichiometry (x = 10, 20, 33.3, 40). It is also emphasized that the term '$CaZrO_3$' in the stoichiometry is used only to indicate the proportion of cations and the perovskite type $CaZrO_3$ phase as such was not involved in any stage of the synthesis process.

Conventional solid-state reaction route was adopted in this work for the synthesis of solid materials. Commercially available $CaCO_3$ (Acros, 99.9%), Gd_2O_3 (Aldrich, 99.9%) and ZrO_2 (Aldrich, 99%) were chosen as the starting materials. The dried powders of the reactants were weighed stoichiometrically and the starting mixture was mixed thoroughly in an agate mortar in acetone medium with intermittent drying to attain maximum homogeneity. The mixtures in pellet form were calcined at first at a temperature of 1300^{o}C for 6 hours. The calcined pellets were ground to fine powder, again made to pellets and were reheated to 1600^{o}C for 6 hours. Dense pellets were prepared by pressureless sintering of pellets at 1650^{o}C for 24 hours. The

green pellets for sintering were made by uniaxial compaction of powder samples at a pressure of 25MPa.

The phase composition of sintered samples at room temperature was analyzed using an X-ray diffractometer (X'pert Pro, PANalytical) employing Cu Kα radiation with a wavelength of 1.5406Å. XRD data were recorded in the 2θ range from 10^o to 90^o. Morphological study was done using a scanning electron microscope (JEOL JSM-5600LV) and a transmission electron microscope (TEM, TECNAI 30G2 S-TWIN, The Netherlands). Finely powdered samples dispersed in acetone by ultrasonication were drop-cast onto carbon-coated copper grids for TEM study. Lattice thermal expansion behaviour was investigated by high-temperature X-ray diffraction analysis (Anton Paar HTK-attachment) Electrical characterization of the sintered pellets was carried out using an impedance analyser (Solartron SI 1260) with a dielectric interface (Solartron 1296), the measurement being done in air in a frequency range from 1 Hz to 1 MHz, from 473 K to 1023 K in intervals of 50 K. Electroding was facilitated by painting silver paste over the flat polished surfaces of the cylindrical pellets. Silver wires were used to connect the samples to the frequency response analyzer via the dielectric interface.

3. Results and Discussion:

The proposed chemical compositions consisted of *x*% of $CaZrO_3$ and *(100-x)*% of $Gd_2Zr_2O_3$ in their stoichiometry, *x* being 0, 10, 20, 33 and 40 for different samples. Such a stoichiometry assumed substitution of Gd^{3+} by Ca^{2+} due to their similar ionic radii and the difference in valence of these two ions could introduce anionic vacancies in the lattice. The solid state reaction route yielded powder samples which were then sintered at 1650°C. For structural studies like X-ray diffraction and transmission electron microscopy the sintered samples were ground to form fine powder, while the pellets as such were used for scanning electron microscopy and impedance spectroscopy studies.

3.1. Structural studies:

X-ray diffraction study of powdered samples was primarily used to investigate the crystal structure of the samples. The peak patterns, in general, were found to be typical of the cubic fluorite structure (ICDD pattern code: 00-016-0799). The CGZ 40 composition showed minor secondary phase reflections that are not characteristic of cubic fluorites. These impurity peaks indicated by asterisks in Figure 1 were corresponding to the perovskite type structure of $CaZrO_3$. It implied a limit up to which $CaZrO_3$ can be stoichiometrically added to $Gd_2Zr_2O_7$ without compromising the phase purity of the crystal lattice.

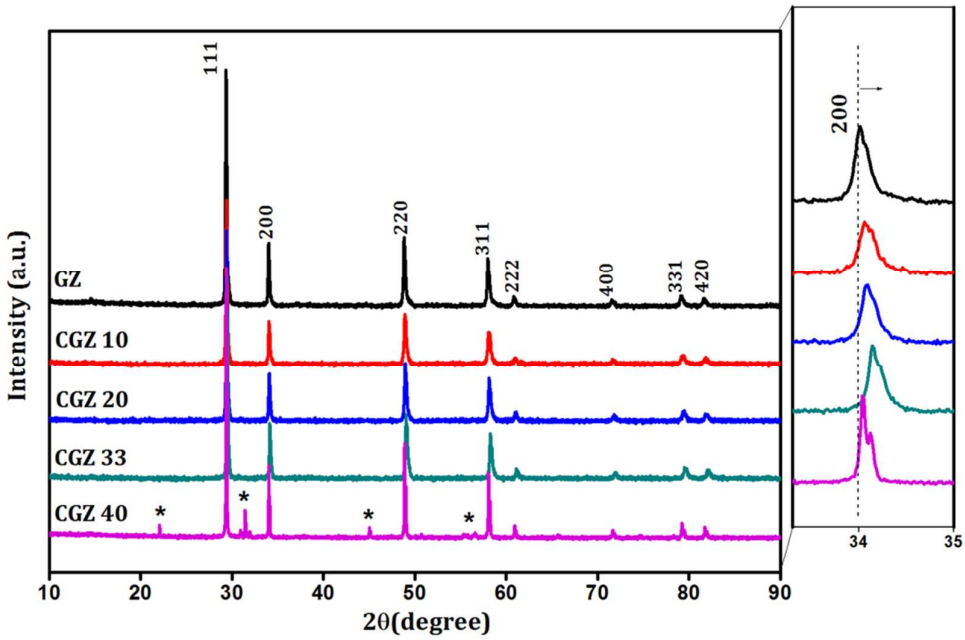

Figure 1: Powder X-ray diffraction patterns of various samples. Side panel shows the expanded view of the (200) reflection at ~34°

A close examination of the qualitative aspects of the patterns shows a shift of peaks towards higher angles with increase in amount of $CaZrO_3$, as evident in the right panel of Figure 1 which is an expanded view of the (200) reflection. The figure also indicates that the CGZ 40 sample falls off this trend which should obviously be due to the considerable amount of impurity phase formation.

Table 1: Starting model for Rietveld simulation and refinement

Sample	GZ	CGZ 10	CGZ 20	CGZ 33
Space group	Fm-3m	Fm-3m	Fm-3m	Fm-3m
Lattice constant	5.2	5.2	5.2	5.2
Wyckoff positions:				
Ca	-	4a	4a	4a
Gd, Zr	4a	4a	4a	4a
O	8c	8c	8c	8c
Site Occupancy:				
Ca	0	0.026	0.056	0.100
Gd	0.500	0.474	0.444	0.400
Zr	0.500	0.500	0.500	0.500
O	0.875	0.870	0.860	0.850

For a detailed analysis of the powder X-ray diffraction results, Rietveld simulation and refinement was carried out using commercially available X'pert Highscore plus software. The standard ICDD file matching the observed peak pattern and the stoichiometry proposed for the preparation of samples were used to construct starting models for the simulation and are listed in the Table 1. A pseudo-Voigt profile function was used to fit the diffraction pattern. The Caglioti parameters and asymmetry parameters were refined along with the flat background polynomial and one of the coefficients and the refined parameters are listed in Table 2.

Table 2: Refined values of various parameters from Rietveld analysis

Sample	GZ	CGZ 10	CGZ 20	CGZ 33
Phase	Fluorite	Fluorite	Fluorite	Fluorite
Unit cell	Cubic	Cubic	Cubic	Cubic
Space group	Fm-3m	Fm-3m	Fm-3m	Fm-3m
Lattice constant, *a* (Å)	5.26897(8)	5.26237(8)	5.25662(6)	5.24707(6)
Flat background	177.7967	159.2650	161.3220	160.8333
Coefficient 1	-28.3843	-1.1223	-5.4340	-4.9942
U	0.1545	0.3508	0.1099	0.1001
V	-0.0257	-0.0736	0.0245	0.0251
W	0.0074	0.0144	-0.0019	-0.0026
R_p (%)	6.58	6.70	6.10	6.10
R_{exp} (%)	6.85	7.43	7.37	7.36
R_{wp} (%)	8.76	8.87	7.87	7.96
GOF	1.63	1.42	1.13	1.16

It can be seen that the lattice parameter decreased progressively with increasing amount of $CaZrO_3$ added, as shown in Figure 2. This trend is counterintuitive considering the ionic radii of the various cationic species involved. Under eight-coordination, as in the case of fluorite-type structures, the ionic radii of Ca^{2+}, Gd^{3+} and Zr^{4+} are 1.12 Å, 1.053 Å and 0.84 Å respectively.[23] The Ca ions can thus be assumed to occupy the Gd site due to their similar ionic radii. The introduction of larger Ca ions in place of Gd ions is expected to expand the lattice in accordance with Vegard's law[24] which is a commonly observed trend in many similar substitutions.[25-27] Here in the present system, the decrease in the fundamental lattice vector of the system can be attributed to the Coulomb considerations when a trivalent cation is substituted by a divalent one. The condition of charge neutrality would require a few oxygen ions to be removed, in effect introducing anion vacancies in the lattice that would in turn lead to a lattice contraction. From stoichiometry, it could be found that, for the upper limit of substitution (x = 33.3%), Ca ions occupy around 20% of the sites previously occupied by Gd ions. Zr^{4+} ions are known to have a tendency to get coordinated by more than six oxygen ions and this in turn is reported as the reason for Zr-containing compositions to have

a stronger tendency to form and retain a defect fluorite structure.[28] A perovskite-type structure like $CaZrO_3$ has only six-coordinated B cations and so its formation as a secondary phase will not be favoured much. This makes it possible to add more Ca^{2+} to the lattice without the formation of secondary $CaZrO_3$ phase in this case, thereby increasing the vacancy concentration. Hence it could be inferred that the effect of oxygen vacancies is dominating over that of ionic size in determining the lattice volume of the present system, as was reported by Sayed et al in a similar chemical systm.[16]

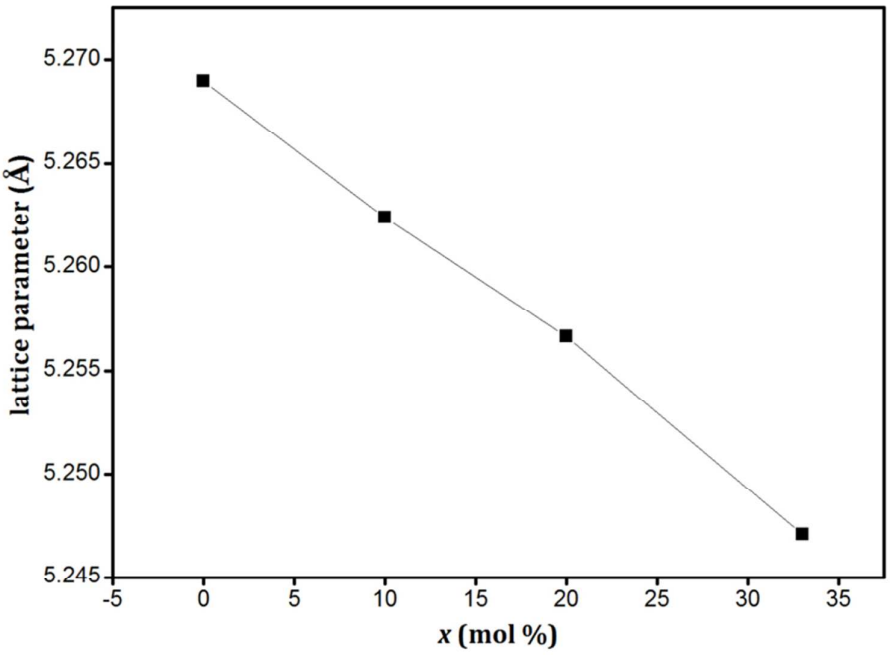

Figure 2: Variation of lattice parameter with mol% of $CaZrO_3$

This could be corroborated by the study of lattice thermal expansion which will be discussed in one of the coming sections. Beyond the solubility limit, the Ca ions tend to take part in the formation of $CaZrO_3$ secondary phase without creating oxygen vacancies in the lattice and hence the fluorite phase attains a larger lattice parameter. Although a good Rietveld refinement for CGZ 40 could not be achieved due to the presence of $CaZrO_3$ impurity peaks, this can be qualitatively observed in Figure 1 where the (200) peak swerve away from the

trend beyond 33%. The result of refinement of a representative sample (CGZ 33) along with the difference plot is shown in Figure 3 which shows that the refinement leads to good agreement between calculated and observed patterns.

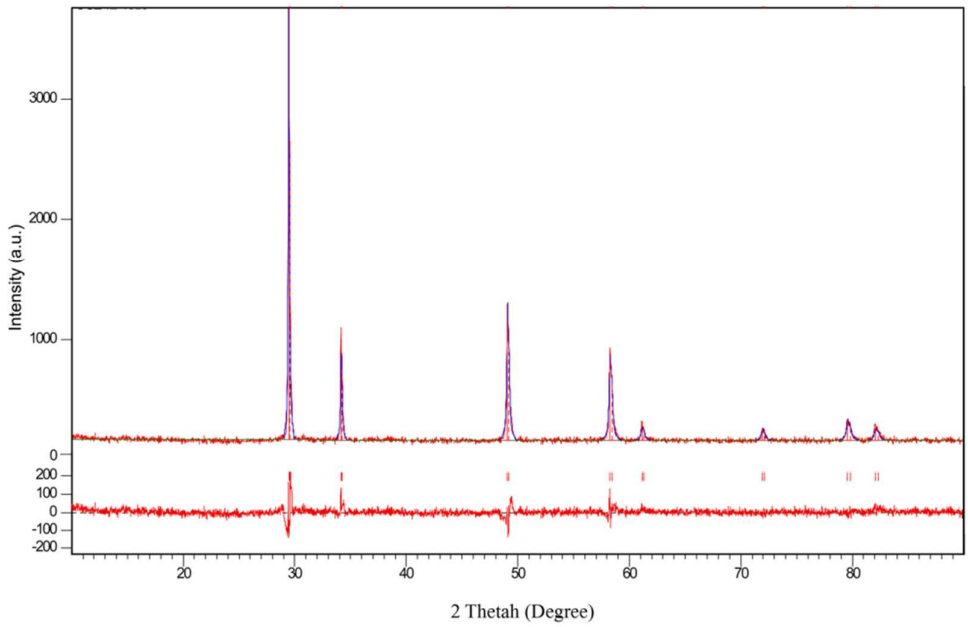

Figure 3: Graphical output of Rietveld refinement of representative sample CGZ 33

3.2. Morphological studies:

The crystalline nature in small microdomains ccan be observed with the aid of transmission electron microscopy whereas powder X-ray diffraction gives an idea about the average crystalline nature. The TEM images of the representative samples are shown in Figure 4. The high resolution images of the lattice clearly showed the (111) Miller planes of a fluorite structure which have a spacing of 0.303 nm. The selected area electron diffraction (SAED) pattern of the representative sample (CGZ 33) showed diffraction rings characteristic of a typical polycrystalline material. The bright spots associated with the rings could be indexed

with (002), (022), (222) and (024) Miller indices the planes corresponding to which could not be distinguished in the HR images of the morphology.

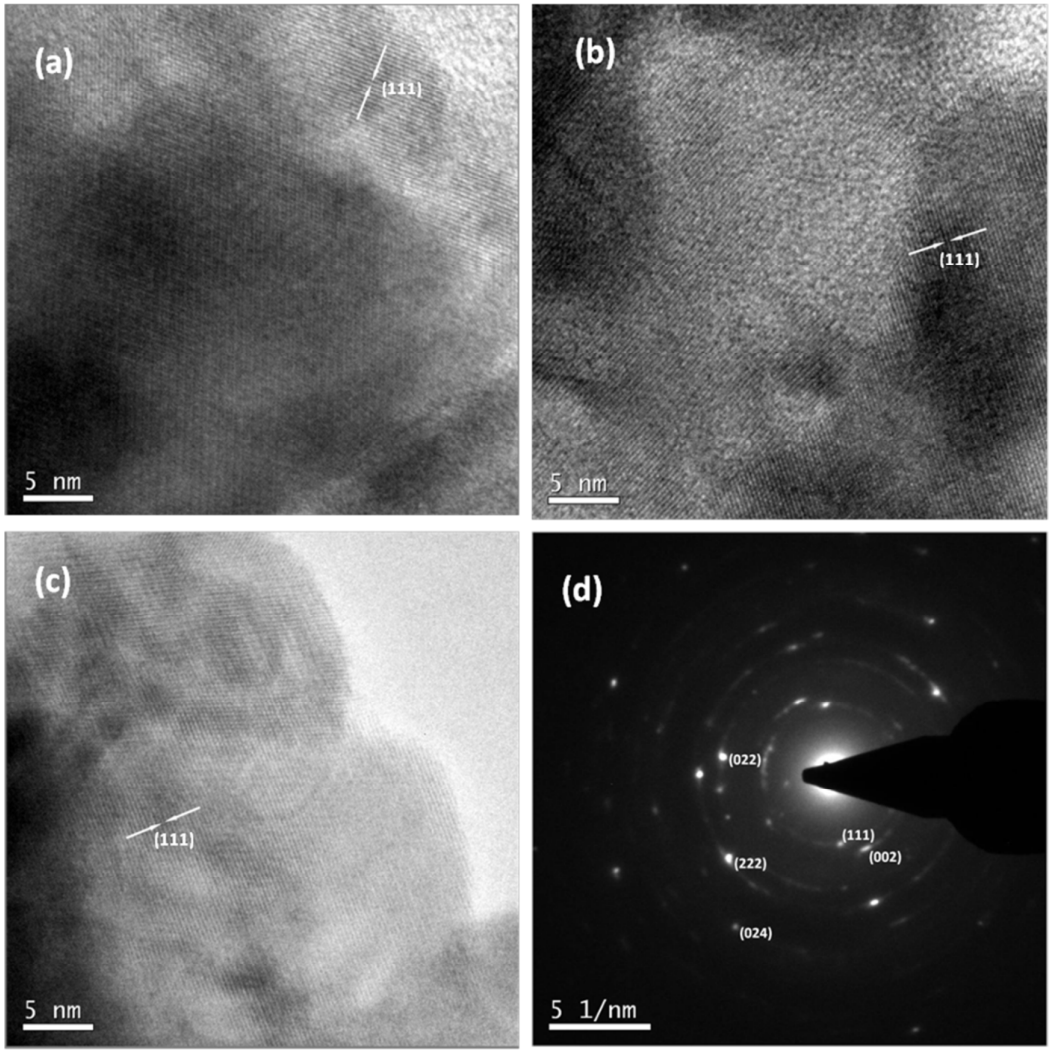

Figure 4: The high resolution TEM images of various samples sintered at 1923 K for 24 hours (a) CGZ 10 (b) CGZ 20 (c) CGZ 33 (d) SAED pattern of CGZ 33

The morphology of the sintered pellets was analyzed using scanning electron microscopy technique. The SEM images of the surfaces of various pellet samples are shown in Figure 5.

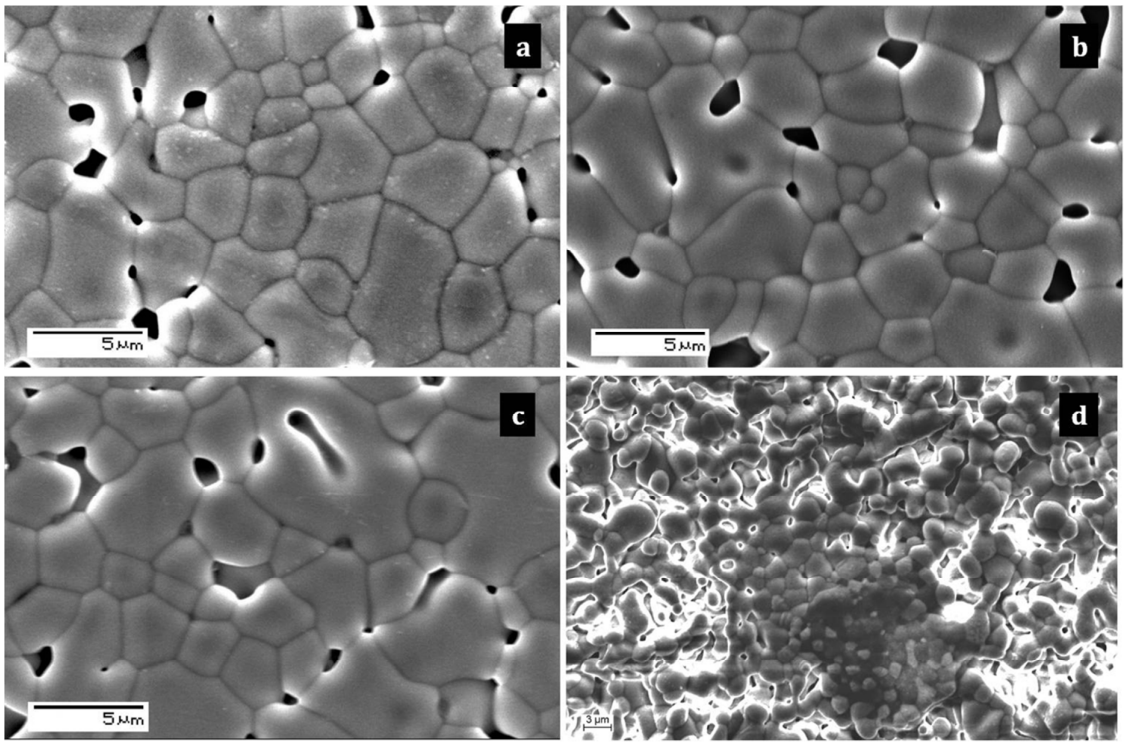

Figure 5: Scanning electron micrographs of the surface of various sample pellets (a) CGZ 10 (b) CGZ 20 (c) CGZ 33 (d) CGZ 40 (unpolished)

The polycrystalline samples are seen to possess grains that are typically in micrometer range of size. Surface of CGZ 40 shows regions that are slightly different in morphology from the surroundings. Distinct grain boundaries can also be seen along with some amount of porosity. The bulk density of various samples as a percentage of their respective theoretical densities is shown in Table 3 below.

Table 3: Bulk densities of various samples

Sample code	Bulk density (% of theoretical density)
GZ	82.4
CGZ 10	82.8
CGZ 20	81.6
CGZ 33	82.5
CGZ 40	83.3

3.3 Thermal expansion studies:

A study of response of a crystal lattice to change in temperature can throw light on to some more aspects of its structural characteristics. The lattice thermal expansion behaviour of the samples was studied by high-temperature X-ray diffraction in a temperature range from ambient temperature to 1273 K at regular intervals of 200 K. Figure 6 shows the X-ray diffraction pattern of the representative sample CGZ 33 at various temperatures in the 2θ range of 28° to 35°. It can be observed that as the temperature increases, the reflections progressively move towards lower angles implying a corresponding expansion of the crystal lattice. It is to be inferred that all the samples showed the typical behaviour of a real anharmonic lattice wherein the pressure of the phonon gas is temperature dependant. It could also be observed that all the samples retained their crystal structure at all temperatures without undergoing any temperature-induced structural transition.

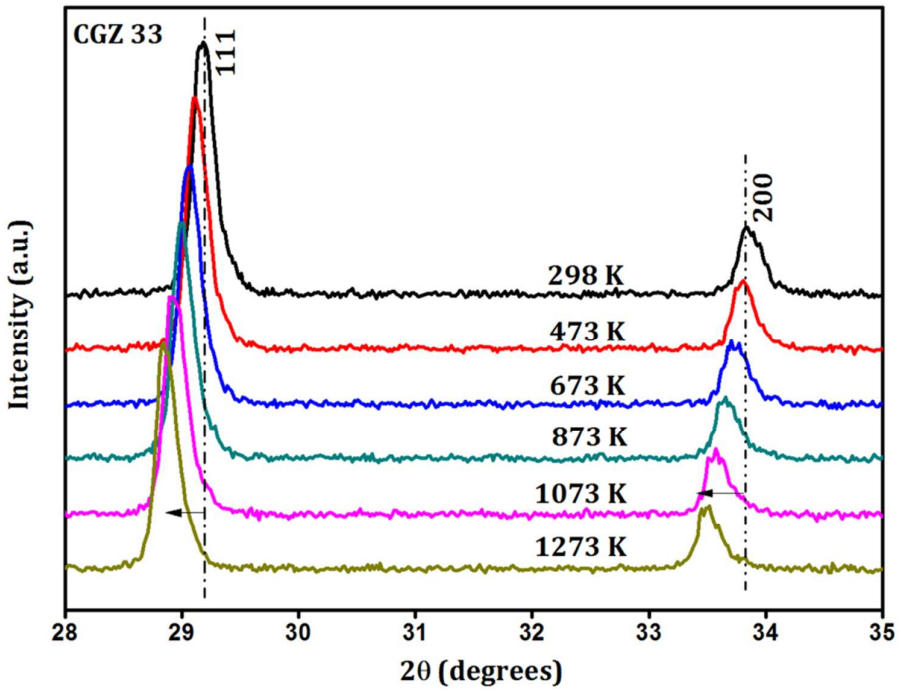

Figure 6: Powder XRD pattern of CGZ 33 at various temperatures (only two reflections being shown for legibility)

The XRD patterns of each sample at all temperatures were analyzed by Le-Bail fitting method carried out in commercially available X'Pert HighScore plus software and the values of lattice parameter were thus calculated from the fitting. The lattice parameter of each sample showed a linear increase with increase in temperature as was already evident in the qualitative inspection of their X-ray diffraction patterns. The lattice thermal expansion coefficients were calculated from the plots of lattice parameter against absolute temperature using the equation

$$\alpha = 1/a_{298}(da/dT)\ K^{-1}$$

Here α is the lattice thermal expansion coefficient, a_{298} is the value of lattice parameter at ambient temperature (298 K) and da/dT is the rate of increase of lattice parameter with temperature. The variation of lattice thermal expansion coefficient is shown in Figure 7 where it can be seen that it increases with increase in mol percentage of $CaZrO_3$ present.

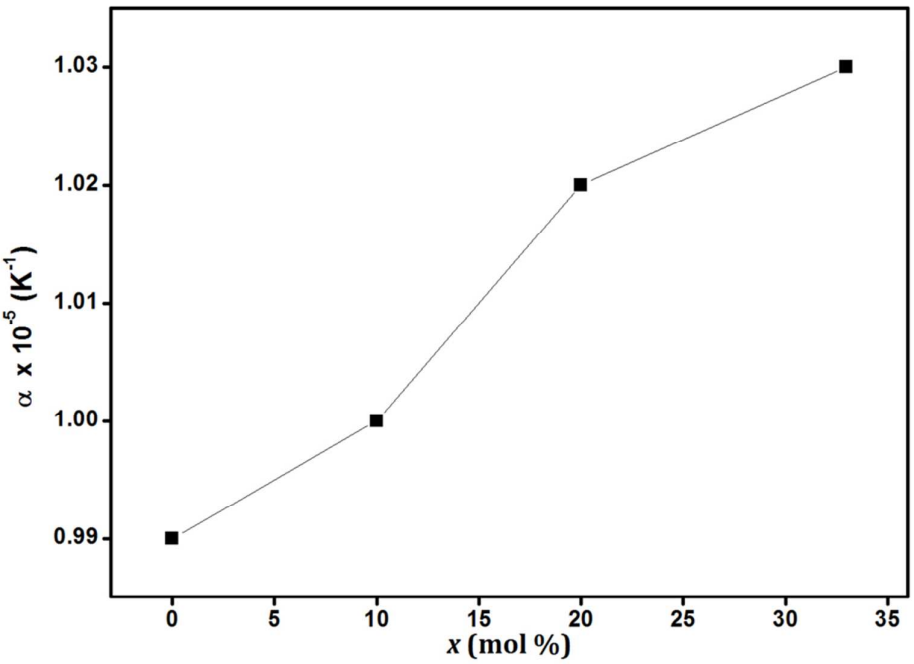

Figure 7: Variation of thermal expansion coefficient with mol% of $CaZrO_3$

It is widely reported that generation of oxygen vacancies is often accompanied by an increase in thermal expansion coefficient.[20-22, 29] The same can be assumed to be a crucial factor in deciding the trend seen in Figure 7 too, since the effect of oxygen vacancies has already been evident in the discussion on lattice parameter in an earlier section. Another aspect of this trend is the change in covalency of the of the average A-O bond in the present system due to the partial substitution of cations by a more electronegative species in the A-site. The difference in electronegativity is a crucial parameter which decides the covalency and strength of a bond between two atoms. Under normal conditions, higher the difference in electronegativity, stronger the bond tends to be.[21] Also, the thermal expansion coefficient of materials is generally reported to increase with increase in bond strength.[22] The Pauling scale electronegativity values of Ca^{2+}, Gd^{3+} and O^{2-} are 1.00, 1.20 and 3.44 respectively.[30] In the scenario where a part of Gd ions are being substituted by Ca ions, which have a lower electronegativity, the strength of average A-O bond is expected to decrease which in turn can decrease the thermal expansion coefficient. But the opposite trend observed in this system corroborates the dominance of oxygen vacancies in deciding its structural properties.

3.4. Electrical studies:

The electrical characteristics were probed via ac impedance spectroscopy technique by investigating the response of sintered pellets to a small ac stimulus (100 mV). The real and imaginary parts of ac impedance as a function of frequency was measured in the temperature range of 473 K to 1023 K and a frequency range of 1 Hz to 1 MHz. The sintered pellets had a density of around 85% of the theoretical density. The typical semicircle response of CGZ 33 for the impedance function is shown in Figure 8. Two distinct semicircular arcs could be observed for all the samples in intermediate temperatures, each of them corresponding to two different mechanism of ionic transport within the material.

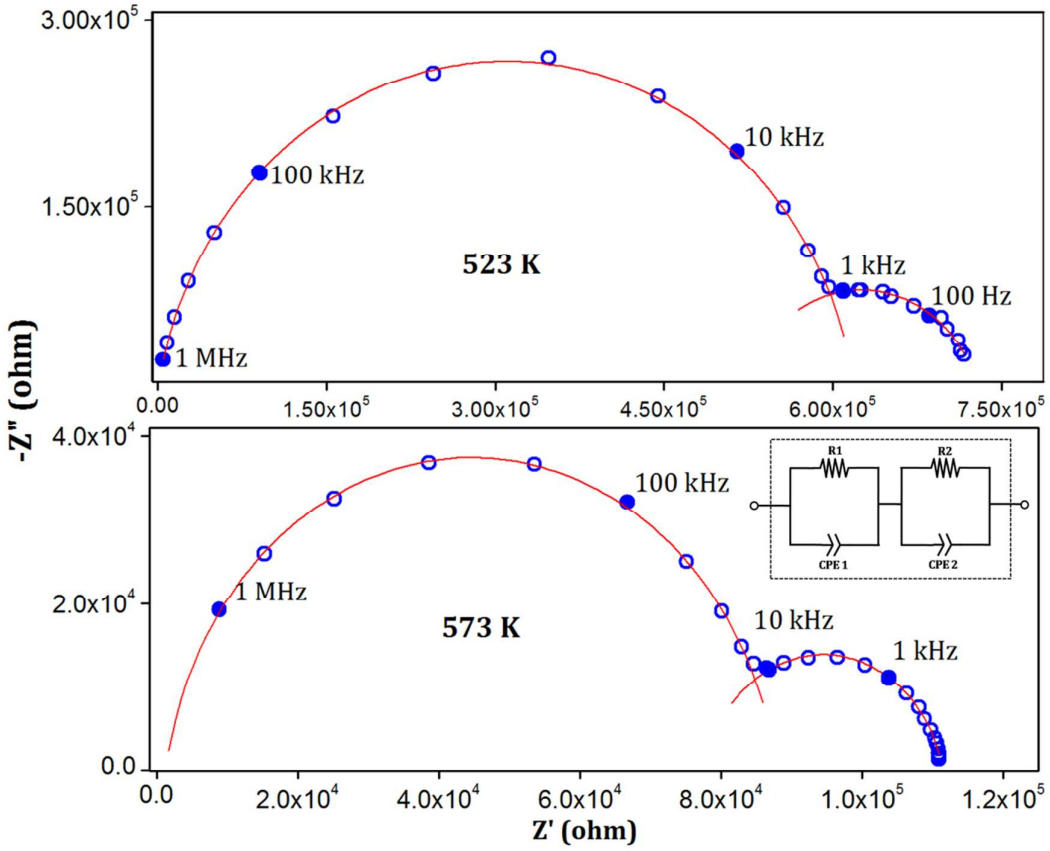

Figure 8: Complex plane representation of ac impedance of CGZ 33 at two temperatures

By calculating the capacitance associated with a particular arc, we can have an idea about the mechanism responsible for it. At the grain boundaries, where there is larger probability of charges being accumulated, the capacitance typically falls in the nanofarad (nF) range and within the grains it is only in picofarads (pF).[3] The intercepts of the arcs with the real axis would yield the value of resistance, R from which the conductivity of the materials can be calculated using the relation,

$$\sigma = l/RA$$

where σ is the conductivity, l is the thickness of the pellet and A is the electroding surface area. At higher temperatures mostly only a vertical spike could be seen (figure not included) making it difficult to resolve the bulk and grain boundary contributions. This is a typical

behaviour for ionic conducting materials and is a result of the high electrode blocking capacitance which usually falls in the microfarad region.[31-34] Hence only the total resistance which is the sum of grain and grain boundary resistances was considered to derive the values of conductivity.

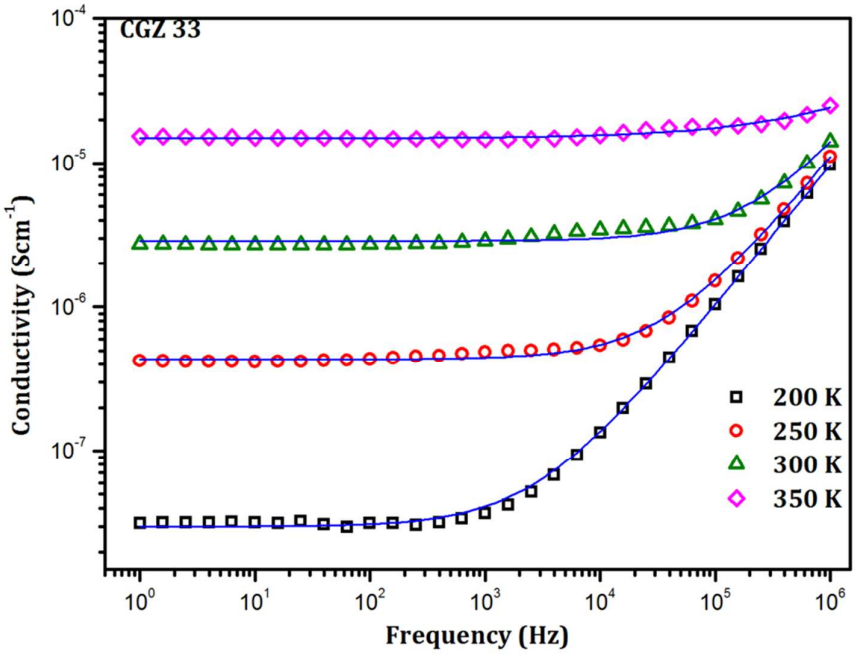

Figure 9: Dispersion of ac conductivity of CGZ 33 at different intermediate temperatures

Figure 9 shows the variation of ac conductivity of CGZ 33 with the applied frequency for a few different temperatures. The plots are characterized by the presence of a frequency-independent plateau and a frequency-dependant positive slope region of conductivity dispersion. This can be found to obey the Jonscher's power law equation,[35]

$$\sigma(\omega) = \sigma_0 + A\omega^n$$

where σ_0 is the frequency-independent conductivity (dc conductivity), A is a temperature dependent constant determined by the strength of polarizability, and n ($0 \leq n \leq 1$) is a constant that depends on the degree of interaction between the mobile ions and the lattice and also on the temperature. This trend of conductivity is an indication that the conduction

mechanism in these materials is through the hopping of ions presumably through the vacant sites introduced in the lattice. It can be seen that the frequency at which dispersion begins to dominate shifts towards higher frequencies when the temperature increases. This may be correlated with the jump relaxation model, according to which the increase in hopping frequency of the carrier species with increase in temperature causes the dispersion to dominate in higher frequencies.[36, 37]

Although the frequency dependent properties of a solid can be expressed in terms of many parameters, complex impedance (Z^*) and the electric modulus (M^*) are generally preferred for materials showing more long range conductivity than dielectric behaviour. Electric modulus is the inverse of dielectric permittivity (ε^*) and can be expressed as,

$$M^* = j\omega C_0 Z^* = M' + jM''$$

where C_0 is the capacitance, Z^* is the complex impedance, M' and M'' are the real and imaginary components of the electric modulus respectively.[37]

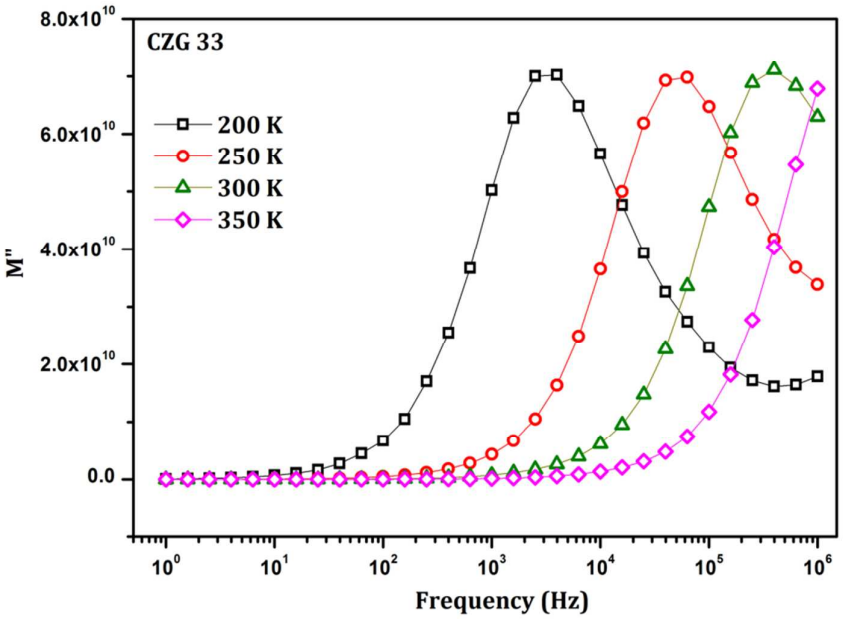

Figure 10: Relaxation of imaginary part of the electric modulus at different intermediate temperatures

Figure 10 shows a plot of imaginary part of electric modulus against frequency. At the low frequency region, value of modulus tends to be zero for all temperatures since it does not receive any significant contribution from the electrode polarization effect. *M"* also shows characteristic peaks at a particular frequency which shifts towards higher frequencies as the temperature is increased. A peak in any dielectric function with respect to frequency is an indication of a relaxation behaviour, the position of which would depend on which function we choose to plot.[38] This behaviour is a generally reported one in oxide ionic conductors[39-41] and can be attributed to the charge re-orientation relaxation of ions involving the vacancies. The shift of this peak towards high frequencies with increase in temperature indicates that the process is thermally activated, the same being also apparent in the decrease in radii of the complex impedance arcs with increase in temperature. Thus the thermally activated ion hopping process can be thought to be responsible for the overall conductivity of these materials.

The temperature dependence of the total conductivity is usually described by the Arrhenius equation,

$$\sigma = (\sigma_o / T) \exp(-E_a/k_B T)$$

Here σ is the conductivity, σ_o is the pre-exponential part corresponding to the availability of effective charge carriers in the system, E_a is the activation energy for the thermally activated conduction, T is the absolute temperature and k_B is the Boltzmann constant. Figure 11 shows a plot of $\log_e(\sigma T)$ against 1000/T, the straight lines being the least squares mathematical fits of the points. These straight line fits show the correspondence of conductivity data with the linearized form of the Arrhenius equation and it delineates the fact that the conduction mechanism in the present study is a thermally activated one.

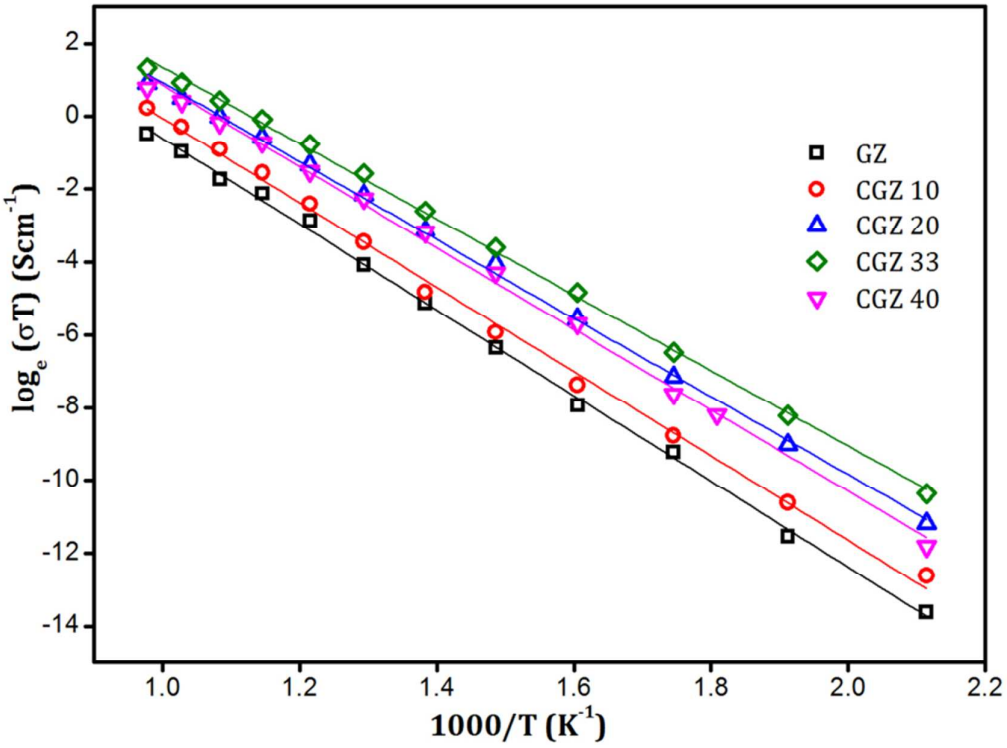

Figure 11: Arrhenius plots of various samples along with their linear fits

The activation energy can be deduced from the slopes of the Arrhenius fits. A plot of activation energy and conductivity at 1023 K against the mol% of $CaZrO_3$ is shown in Figure 12. With an increase in *x*, the activation energy for conduction decreases resulting in an almost linear increase of conductivity up to x = 33.3%. Beyond this limit the activation energy increases and the conductivity decreases. This shows that the conducting property is enhanced by the oxygen vacancies introduced in the lattice by the Ca ions thereby providing a lower energy barrier for the ionic diffusion. The setback in this enhancement beyond a limit can be attributed to the presence of poorly conducting $CaZrO_3$ secondary phase which would create a higher energy barrier as implied by the increase in activation energy for x = 40%.

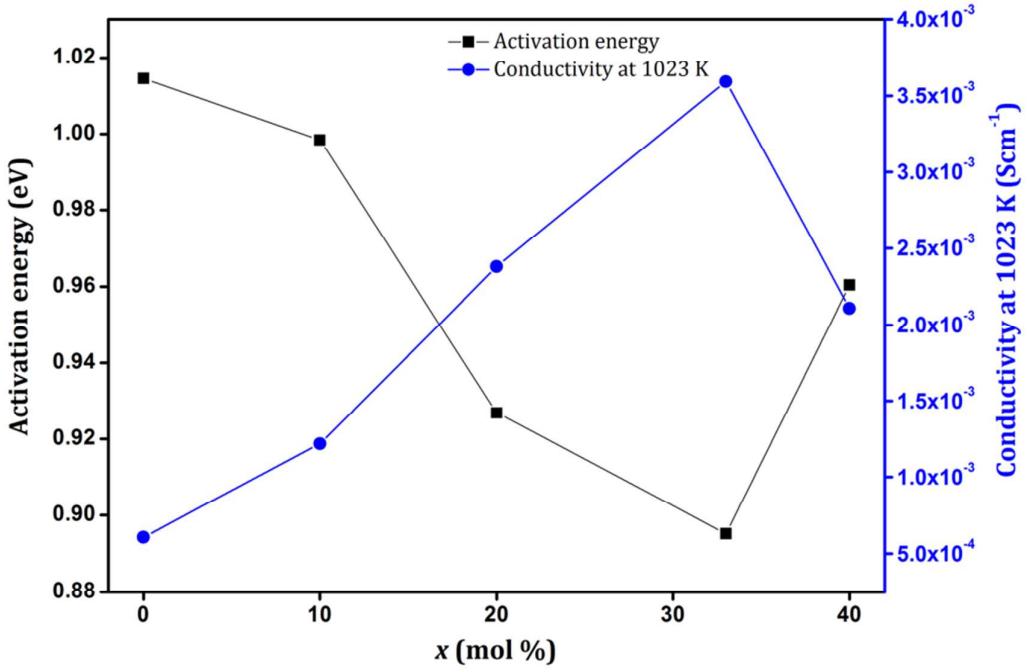

Figure 12: Variation of activation energy and conductivity at 1023 K with mol% of $CaZrO_3$

The maximum value of conductivity obtained in this study is 3.59 $x10^{-3}$ Scm^{-1} at 1023 K. An improvement in the sintering density, which constitutes a future follow up of this work, is expected to improve the conducting properties of these materials making them more potential candidates to be used in solid oxide fuel cell applications.

4. Conclusions

$CaZrO_3$-$Gd_2Zr_2O_7$ solid solutions were crystallized into a cubic fluorite structure. The effect of substitution was to create oxygen vacancies within the lattice that lead to a progressive contraction in the lattice parameter, dominating over the effect of ionic radii difference. The increase in thermal expansion coefficient also implied the dominance of oxygen vacancies. The thermally activated conduction process in these materials was found to follow Arrhenius behaviour and an analysis of dielectric functions was found to indicate an ionic hopping mechanism leading to long range conductivity. The ionic conductivity was enhanced by the substitution due to the lower energy barriers introduced by the oxygen vacancies towards the charge transport. Presence of $CaZrO_3$ secondary phase was seen to be detrimental to conduction process and thus within the limit of solubility, $CaZrO_3$ enhances the electrical conductivity of $Gd_2Zr_2O_7$.

Acknowledgment:

One of the authors, Vaisakhan Thampi, wishes to acknowledge University Grants Commission (UGC, India) for providing financial support.

References:

1. A. Shlyakhtina and L. Shcherbakova, *Russ. J. Electrochem*+, 2012, **48**, 1-25.
2. Z.-G. Liu, J.-H. Ouyang, Y. Zhou, J. Xiang and X.-M. Liu, *Materials & Design*, 2011, **32**, 4201-4206.
3. Z. G. Liu, J. H. Ouyang and K. N. Sun, *Fuel Cells*, 2010, **10**, 1050-1056.
4. Z.-G. Liu, S. Gao, J.-H. Ouyang and X.-L. Xia, *Journal of Alloys and Compounds*, 2010, **506**, 868-871.
5. K. J. Moreno, M. A. Guevara-Liceaga, A. F. Fuentes, J. García-Barriocanal, C. León and J. Santamaría, *J. Solid State Chem.*, 2006, **179**, 928-934.
6. M. Kumar, M. A. Kulandainathan, I. A. Raj, R. Chandrasekaran and R. Pattabiraman, *Mater. Chem. Phys.*, 2005, **92**, 295-302.
7. A. N. Radhakrishnan, P. P. Rao, K. S. M. Linsa, M. Deepa and P. Koshy, *Dalton Trans.*, 2011, **40**.
8. V. Kharton, E. Tsipis, A. Yaremchenko, N. Vyshatko, A. Shaula, E. Naumovich and J. Frade, *J. Solid State Electrochem.*, 2003, **7**, 468-476.
9. O. Porat, C. Heremans and H. L. Tuller, *Solid State Ionics*, 1997, **94**, 75-83.
10. X.-L. Xia, J.-H. Ouyang and Z.-G. Liu, *J. Am. Ceram. Soc.*, 2010, **93**, 1074-1080.
11. Z.-G. Liu, J.-H. Ouyang, K.-N. Sun and Y. Zhou, *J. Power Sources*, 2012, **210**, 96-100.
12. Z.-G. Liu, J.-H. Ouyang, Y. Zhou and X.-L. Xia, *J. Power Sources*, 2008, **185**, 876-880.
13. Y. H. Lee, H. S. Sheu, J. P. Deng and H. C. I. Kao, *J. Alloy. Compd.*, 2009, **487**, 595-598.
14. Z.-G. Liu, J.-H. Ouyang, K.-N. Sun and Y. Zhou, *Ceram. Int.*, 2012, **38**, 2935-2941.
15. X.-L. Xia, J.-H. Ouyang and Z.-G. Liu, *J. Power Sources*, 2009, **189**, 888-893.

16. F. N. Sayed, B. P. Mandal, D. Jain, C. G. N. S. Pillai and A. K. Tyagi, *J. Eur. Ceram. Soc.*, 2012, **32**, 3221-3228.

17. A. V. Shlyakhtina, D. A. Belov, A. V. Knotko, I. V. Kolbanev, A. N. Streletskii, O. K. Karyagina and L. G. Shcherbakova, *Inorg. Mater.*, 2014, **50**, 1035-1049.

18. H. Inaba and H. Tagawa, *Solid State Ionics*, 1996, **83**, 1-16.

19. M. Mogensen, N. M. Sammes and G. A. Tompsett, *Solid State Ionics*, 2000, **129**, 63-94.

20. J. W. Stevenson, K. Hasinska, N. L. Canfield and T. R. Armstrong, *J. Electrochem. Soc.*, 2000, **147**, 3213-3218.

21. J.-X. Wang, L.-P. Li, B. J. Campbell, Z. Lv, Y. Ji, Y.-F. Xue and W.-H. Su, *Mater. Chem. Phys.*, 2004, **86**, 150-155.

22. Masashi Mori, Yoshiko Hiei, Nigel M. Sammes and G. A. Tompsett, *J. Electrochem. Soc.*, 2000, **147**, 1295-1302.

23. R. Shannon, *Acta Cryst. A*, 1976, **32**, 751-767.

24. L. Vegard, *Zeitschrift für Physik*, 1921, **5**, 17-26.

25. J. A. Díaz-Guillén, A. F. Fuentes, M. R. Díaz-Guillén, J. M. Almanza, J. Santamaría and C. León, *J. Power Sources*, 2009, **186**, 349-352.

26. F. N. Sayed, D. Jain, B. P. Mandal, C. G. S. Pillai and A. K. Tyagi, *RSC Adv.*, 2012, **2**, 8341-8351.

27. X.-L. Xia, Z.-G. Liu, J.-H. Ouyang, S. Gao and X.-M. Liu, *Solid State Sci.*, 2011, **13**, 1328-1333.

28. A. Seifert, F. F. Lange and J. S. Speck, *J. Materials. Res.*, 1995, **10**, 680-691.

29. H. Hayashi, M. Suzuki and H. Inaba, *Solid State Ionics*, 2000, **128**, 131-139.

30. D. R. Lide, ed., *CRC Handbook of Chemistry and Physics*, 2005.

31. E. Rangasamy, J. Wolfenstine and J. Sakamoto, *Solid State Ionics*, 2012, **206**, 28-32.

32. M. Kotobukia, H. Munakata, K. Kanamura, Y. Sato and T. Yoshida, *J. Electrochem. Soc.*, 2010, **157**, A1076-A1079.

33. V. T. Sumaletha Narayanan, *J. Power Sources*, 2011, **196**, 8085–8090.

34. R. A. Huggins, *Ionics*, 2002, **8**, 300-313.

35. A. K. Jonscher, *Nature*, 1977, **267**, 673-679.

36. K. Funke, *Solid State Ionics*, 1997, **94**, 27-33.

37. A. Kumar Baral and V. Sankaranarayanan, *Appl. Phys. A*, 2010, **98**, 367-373.

38. K. J. Andrew, *J. Phys. D: Appl. Phys.*, 1999, **32**, R57.

39. P. Sarkar and P. S. Nicholson, *J. Am. Ceram. Soc.*, 1989, **72**, 1447-1449.

40. V. S. A. K. Baral, *Physica B*, 2009, **404**, 1674-1678.

41. A. K. Baral and V. Sankaranarayanan, *Appl. Phys. Lett.*, 2009, **94**, 074101.